MOLECULAR GAS DYNAMICS OF THE LENSED WET-MERGER RXSJ1131-1231 AT *Z*=0.654

T. K. DAISY LEUNG AND DOMINIK A. RIECHERS
Department of Astronomy, Space Sciences Building, Cornell University, Ithaca, NY 14853, USA; tleung@astro.cornell.edu

To be submitted to the ApJ

ABSTRACT

We CO($J=2\rightarrow1$) observations with the Plateau de Bure Interferometer. evidence for differential lensing. wet-merger, Dynamical lens modeling the intrinsic dynamics and blah are suggestive of a rotating disk morphology , consistent with previous results based on optical observations.

Subject headings: ISM: molecular – infrared: galaxies – galaxies: mergers – galaxies: starburst – galaxies: evolution

1. INTRODUCTION

In this paper, we explore the ISM properties of the quadruply imaged quasar RXS J113151.62-123158 (hereafter RXJ1131) at $z_{\rm AGN}=0.685$, with an Einstein ring of size 1.″83 in radius. The foreground lensing galaxy is an elliptical galaxy at $z_{\rm L}=0.295$. The redshifts are spectroscopically confirmed by Sluse et al. (2003). A black hole mass estimate of $\rm M_{BH}<2\times10^8 M_\odot$ is also reported based on X-ray observations (Reis et al. 2014).

This paper is structured as follows. In §2 and §3, we outline the details of the observations and data reduction process. In §4, we report the measurements of the CO lines and photometry from optical to radio wavelengths. In §5, we represent our dynamical lens modeling on the CO($J=2\rightarrow1$) data and the physical properties inferred for RXJ1131. In §6, we discuss the results and implications of this study in the context of molecular gas evolution in mergers and massive galaxies. Finally, we summarize the main results of this study and present our conclusions in §7. We use a concordance ΛCDM cosmology throughout this paper, with parameters from the WMAP9 results: H_0 = 69.32 km s^{-1} Mpc^{-1}, $\Omega_{\rm M}$ = 0.29, and Ω_Λ = 0.71 (Hinshaw et al. 2013).

2. OBSERVATIONS

2.1. *PdBI CO($J=2\rightarrow1$)*

Observations of the CO($J=2\rightarrow1$) rotational line ($\nu_{\rm rest}=230.5379938$ GHz; $\nu_{\rm obs}=139.4$ GHz) toward the gravitationally lensed galaxy RXJ1131-1231 at $z_{\rm QSO}=0.658$ were carried out using IRAM Plateau de Bure Interferometer (PdBI; Program ID: S14BX001; PI: D. Riechers). Two observing runs were carried out on 2014 December 06 and 2015 February 05 under good weather conditions in the C and D array configurations, respectively. The 2 mm receivers were used to cover the redshifted CO($J=2\rightarrow1$) line and the underlying continuum emission, employing a correlator setup providing an effective bandwidth of 3.6 GHz and a spectral resolution of 10.0 MHz ($\sim$ 21.5 km s^{-1}). This resulted in 3.75 hours of cumulative six antenna-equivalent on-source time after discarding unusable visibility data. The nearby quasars 1127−145 and 1124−186 were observed every 22 minutes for pointing, secondary amplitude, and phase calibration, and 1055+018 was observed as the bandpass calibrator for both tracks. MWC349 and 3C279 were observed as primary flux calibrators for the C and D array observations, respectively, yielding $\lesssim$15% calibration accuracy.

The GILDAS package was used to reduce and analyze the visibility data which are then imaged and deconvolved using the CLEAN algorithm with "natural" weighting. This yields a synthesized clean beam size of 4.″44 × 1.″95 (PA = 13°). The final rms noise is $\sigma=1.45$ mJy km s^{-1} beam^{-1} over 10 MHz (21.5 km s^{-1}). The continuum image at $\nu_{\rm cont}\sim$139 GHz is created by averaging over all the 3.16 GHz line-free channels. This yields an rms noise of 0.082 mJy beam^{-1}.

2.2. *CARMA CO($J=3\rightarrow2$)*

Observations of the CO($J=3\rightarrow2$) rotational line in RXJ1131 ($\nu_{\rm rest}=345.7959899$ GHz; $\nu_{\rm rest}=209.1$ GHz) were carried out with the Combined Array for Research in Millimeter-wave Astronomy (CARMA; Program ID: cf0098; PI: D. Riechers) in the D array configuration on 2014 February 02 under poor 1.5 mm weather conditions and on 2014 February 17 under good 1.5 mm weather conditions. The correlator setup provides a bandwidth of 3.75 GHz in each sideband and a spectral resolution of 12.5 MHz ($\sim$17.9 km s^{-1}). The line was placed in the lower sideband with the local oscillator tuned to $\nu_{\rm LO}\sim$216 GHz. The radio quasars J1127−189 (first track) and 3C273 (second track) were observed every 15 minutes for pointing, amplitude, and phase calibration. Mars was observed as the primary absolute flux calibrator and 3C279 was observed as the bandpass calibrator for both tracks. This results in a total on-source time of 2.94 hours after flagging poor visibility data.

Given that the phase calibrator used for the first track was faint and was observed under poor weather conditions and that the phase calibrator used for the second track was far from our target source, the phase calibration is subpar, with an rms scatter $\sim$60°over $\sim$135 m. We thus conservatively estimate a calibration accuracy of $\sim$45% based on the flux scale uncertainties, the gain variations over time, and the phase scatter on the calibrated data. We therefore treat its line intensity with caution and ensure that any physical interpretation of this system does not rely on this quantity.

The MIRIAD package was used to calibrate the visibility data which are then imaged and deconvolved using the CLEAN algorithm with "natural" weighting. This yields a synthesized clean beam size of 3.″2 × 1.″9 (PA = 8°) for the lower sideband image cube. The final rms noise is σ = 13.3 mJy km s^{-1} beam^{-1} over a channel width of 25 MHz. An rms noise of σ = 0.83 mJy beam^{-1} is reached by averaging over the line-free channels.

2.3. *VLA (Archival)*

Our analysis also uses archival data of the 5 GHz radio continuum obtained with the Very Large Array (VLA; Program ID: AW741; PI: Wucknitz). Observations were carried out on 2008 December 29 under excellent weather conditions in the A array configurations for a total of ∼7 hours on-source time. The C–band receivers were used with a continuum mode setup, providing a bandwidth of 50 MHz in each sideband. The nearby radio quasar 1130−149 was observed every 10 minutes for pointing, amplitude, and phase calibration, 1331−305 was observed as the primary flux calibrator, and 0319+415 was observed as the bandpass calibrator, yielding ∼10% calibration accuracy. We use AIPS to calibrate the visibility data which are then imaged and deconvolved using the CLEAN algorithm using robust = 0. This yields a synthesized clean beam size of 0.″49 × 0.″35 (PA = 0.″18) and a final rms noise of σ = 13 μJy beam^{-1}.

3. HST ASTROMETRY

We obtained an *HST* image taken with the F555W filter (V-band) using the ACS/Wide Field Camera from the Hubble Legacy Archive[1] with a goal to understand the origin of the emission detected in our mm observations. The details of the observations can be found in Claeskens et al. (2006, hereafter C06). We adopt the VLA 5 GHz map of ∼0.″5 resolution as the reference coordinate frame to align the optical (V-band) image. We shift the latter to the east by 0.″5963 in R.A. and +0.″8372 in Dec., which is consistent with the typical astrometric precision (1″–2″) of images from the Hubble Legacy Archive[2]. This astrometric correction is critical to avoid artificial spatial offsets between different emitting regions and to carry out our lens modeling, in which the absolute position of the foreground lensing galaxy is guided by its coordinates in the optical image, where its emission is clearly detected. The VLA image is calibrated using a well-monitored phase calibrator, with absolute positional accuracy of ∼2 mas. For this reason, the absolute alignment between the VLA image and other interferometric images reported in this paper are expected to have an astrometric precision better than 0.″1, modulo uncertainties related to the SNR, phase instabiliy, and beam size.

[1] Based on observations made with the NASA/ESA Hubble Space Telescope, and obtained from the Hubble Legacy Archive, which is a collaboration between the Space Telescope Science Institute (STScI/NASA), the Space Telescope European Coordinating Facility (ST-ECF/ESA) and the Canadian Astronomy Data Centre (CADC/NRC/CSA).

[2] http://hla.stsci.edu/hla_faq. html

4. RESULTS

4.1. *CO(J = 2 → 1) Emission*

We detected the CO(J = 2 → 1) line emission toward the background galaxies at ≳27σ significance, confirming the redshift at $z_{\rm CO}$ = 0.65370 ± 0.0005. The emission is spatially and dynamically resolved with a highly asymmetric double-horned line profile as shown in Figure 1. Fitting a double Gaussian results in peak flux densities of 75.3 ± 2.6 and 24.0 ± 2.0 mJy, and a FWHM of 179 ± 9 km s^{-1} and 255 ± 28 km s^{-1}, respectively. The peaks are separated by $\Delta v_{\rm sep}$ = 400 ± 12 km s^{-1}. The total integrated line flux is 24.1 ± 2.3 Jy km s^{-1}.

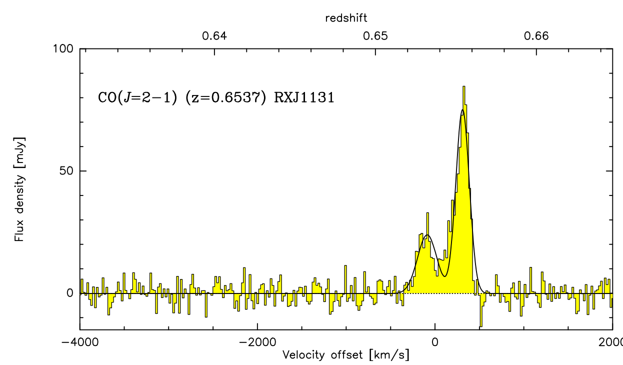

FIG. 1.— Spectrum of CO(J = 2 → 1) emission toward RXJ1131. The velocity scale is with respect to z=0.6537, which is approximately the line center considering the asymmetry as a result of differential lensing. A detailed discussion of this effect is presented in §5.1.2 and the magnification factors for various kinematic components are listed in Table 3.

We construct the zeroth moment map and the renzogram in Figure 2, and the higher-order first and second moment maps in Figure 3 using the uv-continuum subtracted data cube over a velocity range of Δv ∼ 750 km s^{-1}. The renzogram is created using different velocity channels for the blue- and redshifted velocity components and the higher-order moment maps are created using channel maps with 3σ clipping. The peak flux density is 8.12 ± 0.30 Jy km s^{-1} beam^{-1} in the intensity-integrated map.

The deconvolved source size FWHM is estimated to be 5.″1 ± 0.″72 × 3.″72 ± 0.″66, and thus, the emission is resolved over ∼2.2 beams. While the lensed emission is not strictly distributed as two-dimensional Gaussian; the fit recovers the line intensity enclosed by the emitting region, we therefore take this as an estimate on the extent of the lensed emission. On the other hand, if we assume the spatial distribution of the lensed molecular gas emission is similar to that in the optical to near-IR wavelengths, the lensed emission would be more accurately described by an annulus, enclosing the partially complete "Einstein Ring" and the lensed knots (see Figure 2).

We also place an upper limit on HNC(J = 2 → 1) line emission in the foreground galaxy at z ∼0.295. Assuming a typical line width of 300 km s^{-1}, this corresponds to a 3σ limit of 0.35 mJy km s^{-1} beam^{-1}.

4.2. *CO(J = 3 → 2) Emission*

We detect CO(J = 3 → 2) line emission toward RXJ1131 at **BLAH**σ significance. The spectrum is shown in Fig-

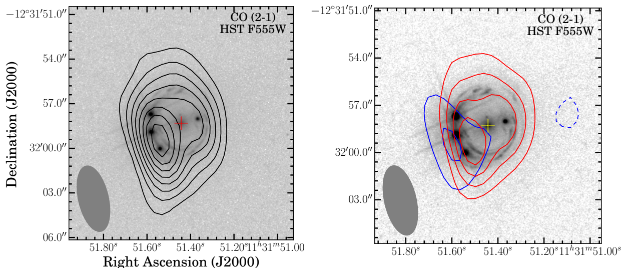

FIG. 2.— Left: an overlay of the velocity-integrated CO($J = 2 \rightarrow 1$) emission on the *HST V*–band (F555W) image. Right: contours are color-coded to represent the red and blue wings of the emission. The contours start at 3σ and increment at steps of $\pm 3\sigma$, where $\sigma = 0.3$ mJy beam^{-1}. The crosses denote the location of the foreground galaxy at $z = 0.295$.

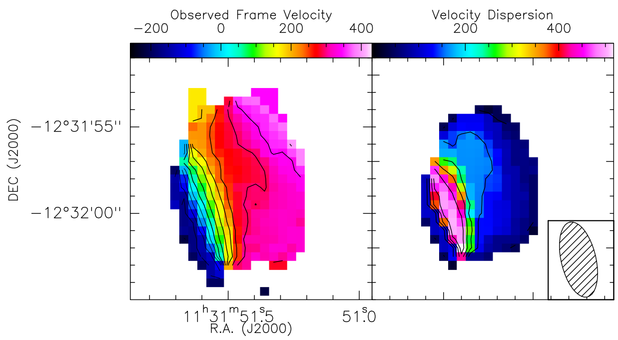

FIG. 3.— Contours for the first (left) and second (right) moment maps are shown in steps of 50 km s^{-1}, and 100 km s^{-1}, respectively. The beam (native resolution) is shown in the right panel.

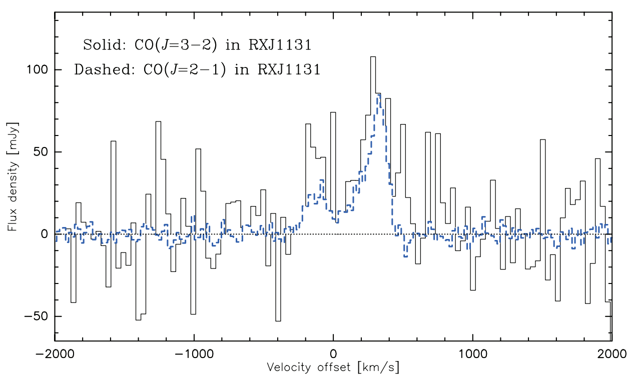

FIG. 4.— CARMA CO($J = 3 \rightarrow 2$) line profile (solid) without continuum subtraction is over-plotted on the continuum-subtracted PdBI CO($J = 2 \rightarrow 1$) line profile (dashed). The velocity scale is with respect to z=0.6537, which corresponds to the dynamical center of the CO($J = 2 \rightarrow 1$) line. The spectral resolution for CO($J = 3 \rightarrow 2$) and CO($J = 2 \rightarrow 1$) is 35.8 km s^{-1} and 21.5 km s^{-1}, respectively.

ure 4, which seems to have a double-peak profile. This is expected if RXJ1131 is truly a disk galaxy (see previous sections). The high phase noise in the calibration leads to a low SNR detection. We thus estimate the line intensity to be 35.7 ± 21.9**BLAH** Jy km s^{-1} by summing up fluxes over the FWZI linewidth used to infer CO($J = 2 \rightarrow 1$) line intensity ($\sim$700 km s^{-1}).

Assuming the spatial extents between CO($J = 2 \rightarrow 1$) and CO($J = 3 \rightarrow 2$) are similar and therefore magnified by the same amount, the line intensities correspond to a brightness temperature ratio of

$$r_{32} = \mathrm{T}_{\mathrm{CO}(J=3\rightarrow2)} / \mathrm{T}_{\mathrm{CO}(J=2\rightarrow1)} = 0.66 \pm 0.41.$$

4.3. *Continuum Emission*

No 1.5 mm continuum emission is detected at the position of CO($J = 3 \rightarrow 2$) down to a 3σ limit of 2.49 mJy beam^{-1}. This is consistent with the spectrum shown in Figure 4.

We detect PdBI 2 mm continuum in Figure 5. The integrated flux density is 1.2 ± 0.2 mJy, with a peak flux $S_\nu = 800 \pm 88\,\mu$Jy beam^{-1} centering on the lensing galaxy. Slightly extended emission is also detected along the lensed arc. This suggests that the detected emission comes from both the foreground galaxy and the background galaxy and that the emission is marginally resolved along its major axis. We subtract a point source model in *uv*-plane to remove the unresolved emission toward the foreground galaxy. The peak flux (0.39 ± 0.08 mJy) in the residual map coincides with the lensed arc, and is consistent with the difference between the integrated and the peak flux in the original continuum map ($\sim$0.4 mJy). We therefore adopt $S_\nu = 0.39 \pm 0.08$ mJy as the 2 mm continuum emission toward the background galaxy.

The VLA C-band continuum image in Figure 5 shows resolved emission from the jets and core of the foreground elliptical galaxy as well as emission toward the background quasar. Multiple peaks are seen along the arc and their centroids coincide with the optical emission from the quasar. We extract the flux densities for the arc and the core in Table 1. We find a spectral index of $\alpha^{2\mathrm{mm}}_{6\mathrm{cm}} = -0.024$ for the foreground galaxy and $\alpha^{2\mathrm{mm}}_{6\mathrm{cm}} = -0.345$ for the background galaxy by fitting a power-law ($S_\nu \propto \nu^\alpha$) to the continuum emission at 5 GHz and 2 mm.

4.4. *Photometry*

We compile mid-IR (MIR) to far-IR broadband photometry from various catalogs available on the NASA/IPAC Infrared Science Archive (IRSA) in Table 1 with aperture corrections when warranted. These data were obtained from the Two Micron All Sky Survey (2MASS; Skrutskie et al. 2006), the Wide-field Infrared Survey Explorer (*WISE*; Wright et al. 2010), the *Infrared Astronomical Satellite* (*IRAS*; Neugebauer et al. 1984), and the Multiband Imaging Photometer (MIPS; Rieke et al. 2004) and Mid-infrared Infrared Array Camera (IRAC; Fazio et al. 2004) on the *Spitzer Space Telescope*. We retrieve PBCD (level 2) *Spitzer*/IRAC images from the Spitzer Heritage Archive and perform aperture photometry on the channel 1 image to extract the flux density at 3.6 μm since it is not available from the IRSA archive.

The emission in the IRAC images is slightly extended. We thus use the *HST* image ($\sim$0$''$.07 resolution) to determine origins of their centroids, all of which are found to be centered at the position corresponding to the lensed emission from the background galaxy. To recover the diffuse background emission, we subtract a point source model centered on the lensing galaxy, using the average FWHM found by fitting a Gaussian profile to several field stars with the IMEXAM routine of IRAF. We perform aperture photometry on the residual image to obtain decomposed

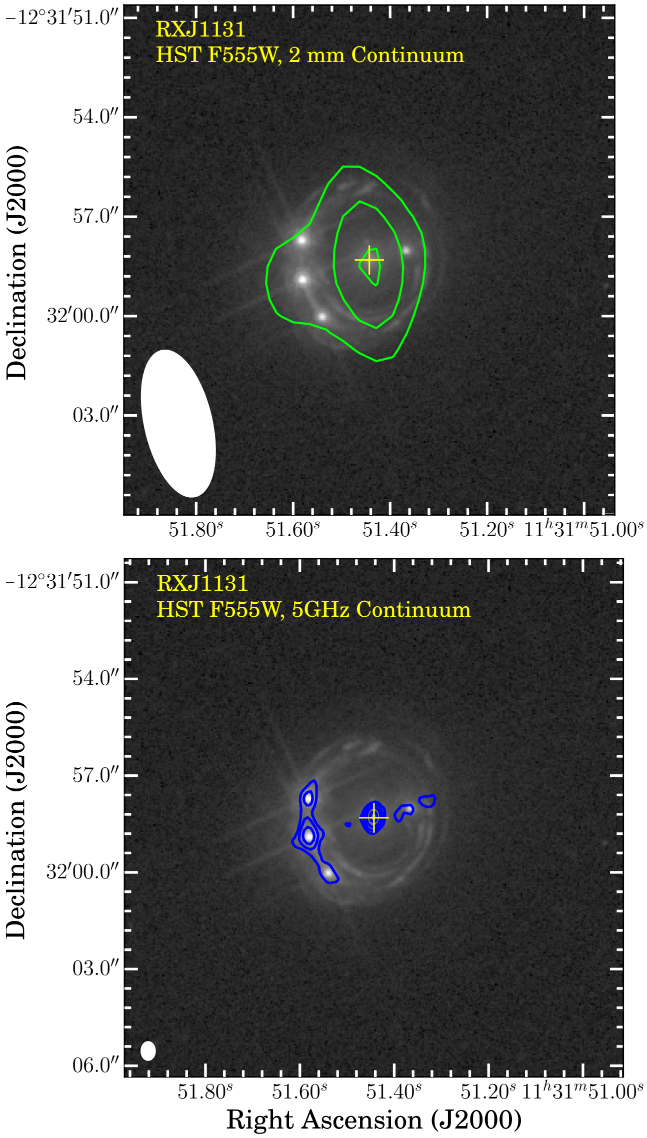

FIG. 5.— Top: an overlay of the 2 mm continuum emission on the optical image. Bottom: VLA 5 GHz continuum emission is overlaid on the optical image. Contours in both images start and increment at steps of $\pm 3\sigma$, where $\sigma_{2\mathrm{mm}} = 0.082$ mJy beam^{-1} and $\sigma_{5\mathrm{GHz}} = 13$ μJy beam^{-1} in the left and right panel, respectively. The central crosses indicate the centroid of the foreground galaxy, as detected in the optical image. The synthesis beams are shown in the bottom left corner of each panel.

flux measurements from the background galaxy. The photometry for the foreground galaxy is then obtained by subtracting the background emission from the observed total flux. The resulting photometry in Table 1 are obtained after performing an aperture correction described in the IRAC Instrument Handbook[3] to correct for the fact that the imaging was calibrated using a 12" aperture, which is larger than the aperture (5.″8) we used to perform aperture photometry.

We fit a power-law spectrum to the decomposed IRAC photometry to disentangle the observed total flux at MIPS 24 μm into the foreground and background galaxies. We find a spectral index of $\alpha \sim -1.8$ and $\alpha \sim -0.85$ for the lensing galaxy and RXJ1131, respectively. This is consistent with the mean $3.6-8\,\mu$m spectral slope of $\alpha = -1.07 \pm 0.53$ found for unobscured AGN (Stern et al. 2005). An extrapolation of the fit to 24μm yields 33.96 ± 0.01 mJy and 25.19 ± 0.03 mJy for the foreground galaxy and RXJ1131, respectively. We note that the IRAC photometry includes emission from old stellar populations and is prone to dust extinction. Hence, the decomposed fluxes are only our best estimate of the warm dust emission. We incorporate the decomposed 24μm point in our SED fitting to provide some constraints on the Wien tail beyond the dust peak of the spectral energy distribution (SED) of RXJ1131. Details of the SED modeling is presented in §5.4.

Extraction of the *Herschel*/SPIRE photometry was carried out using SUSSEXTRACTOR within the Herschel Interactive Processing Environment (HIPE; Ott 2010) on Level 2 maps obtained from the Herschel Science Archive. These maps were processed by the SPIRE pipeline version 13.0 within HIPE. The SUSSEXTRACTOR task estimates the flux density from an image convolved with a kernel derived from the SPIRE beam. The flux density measured by SUSSEXTRACTOR is additionally confirmed using the Timeline Fitter, which performs photometry by fitting a 2D elliptical Gaussian to the Level 1 data at the source position given by the output of SUSSEXTRACTOR. The fluxes obtained from both methods are consistent within the uncertainties.

5. ANALYSIS

5.1. *Lens Modeling*

At the angular resolution of the CO($J = 2 \rightarrow 1$) data, the images are resolved over $\sim$2 resolution elements. Given the extent of the lensed emission, this implies that our CO($J = 2 \rightarrow 1$) observations do not resolve structures (e.g. knots and arcs) of the lensed emission (i.e., sub-optimal for performing lens modeling). Nevertheless, the high spectral resolution of this data provides dynamical information on spatial scales smaller than the beam (see Figure 3). Hence, with the high SNR, we reconstruct the intrinsic gas dynamics by carrying out a parametric lens modeling over different channel slices of the interferometric data using our lensing code UVMCMCFIT (Bussmann et al. 2015; see Bussmann et al. 2015 for details of the code). Models of each slice thus provide the properties on the intrinsic kinematics. To increase the SNR for modeling, the slices are obtained by binning five native channels ($\Delta v \sim 21.5$km s^{-1}) over the full linewidth of $\sim$750 km s^{-1} in the original data, resulting in seven independent channels.

The lens mass distribution is modeled using a singular isothermal ellipsoid (SIE) profile, which is described by five free parameters: the positional offset in R.A. and Dec. relative to an arbitrary chosen fixed coordinate in the image, the Einstein Radius, the axial ratio, and the position angle. We use the VLA radio continuum emission toward the foreground galaxy to initialize the positional offset. We impose a uniform prior $\pm 0.''05$ in both ΔR.A. and ΔDec., motivated by the astrometry uncertainties in

[3] http://irsa.ipac.caltech.edu/data/SPITZER/docs/irac/iracinstrumenthandbook/

TABLE 1
PHOTOMETRY DATA

Wavelength μm	Frequency GHz	Flux Density mJy	Instrument
0.555	540167	0.056 ± 0.006	*HST*-ACS/V-Band (L)
0.555	540167	0.009 ± 0.0041	*HST*-ACS/V-Band (H)
0.814	368295	0.238 ± 0.013	*HST*-ACS/I-Band (L)
0.814	368295	0.041 ± 0.0054	*HST*-ACS/I-Band (H)
1.25	239834	1.009 ± 0.09	2MASS/J-Band
1.6	187370	0.539 ± 0.041	*HST*-NICMOS(NIC2)/H-Band (L)
1.6	187370	0.133 ± 0.004	*HST*-NICMOS(NIC2)/H-Band (H)
1.65	181692	1.448 ± 0.12	2MASS/H-Band
2.17	138153	2.064 ± 0.16	2MASS/Ks-Band
3.4	88174.2	7.027 ± 0.14	*WISE*/W1
3.6	83275.7	5.618 ± 0.0021	*Spitzer*/IRAC
3.6	83275.7	5.034 ± 0.0021	*Spitzer*/IRAC (H)
3.6	83275.7	0.585 ± 0.003 [a]	*Spitzer*/IRAC
4.5	66620.5	7.803 ± 0.0021	*Spitzer*/IRAC
4.5	66620.5	6.009 ± 0.0017	*Spitzer*/IRAC (H)
4.5	66620.5	1.794 ± 0.0027 [a]	*Spitzer*/IRAC
4.6	65172.3	8.872 ± 0.16	*WISE*/W2
5.8	51688.4	10.720 ± 0.0051	*Spitzer*/IRAC
5.8	51688.4	7.557 ± 0.003	*Spitzer*/IRAC (H)
5.8	51688.4	3.163 ± 0.0059 [a]	*Spitzer*/IRAC
8.0	37474.1	14.470 ± 0.0041	*Spitzer*/IRAC
8.0	37474.1	9.881 ± 0.0039	*Spitzer*/IRAC (H)
8.0	37474.1	4.589 ± 0.0057 [a]	*Spitzer*/IRAC
12	24982.7	21.960 ± 0.42	*WISE*/W3
12	24982.7	<400	*IRAS*
22	13626.9	55.110 ± 1.9	*WISE*/W4
24	12491.4	70.204 ± 0.026	*Spitzer*/MIPS
25	11991.7	< 500	*IRAS*
60	4996.54	< 600	*IRAS*
100	2997.92	< 1000	*IRAS*
250	1199.17	289.4 ± 9.6	*Herschel*/SPIRE
350	856.55	168.2 ± 8.6	*Herschel*/SPIRE
500	599.585	56.8 ± 8.8	*Herschel*/SPIRE
1387.93	216	<2.492	CARMA
2152.82	139.256	1.230 ± 0.220	PdBI (integrated)
2152.82	139.256	0.799 ± 0.082	PdBI (peak)
2152.82	139.256	0.400 ± 0.082 [b]	PdBI
61414	4.8815	1.273 ± 0.042	VLA/Cband (arc)
61414	4.8815	0.866 ± 0.027	VLA/Cband (core)

REFERENCES. — The *HST* photometry is taken from C06.

NOTE. — (H) and (L) in column 4 indicate the flux (in column 3) of RXJ1131 and its lensing galaxy, respectively. The IRAC photometry at 3.6μm is extracted directly from the image and from the Spitzer Heritage Archive for channels 2–4 (4.5, 5.8, and 8.0μm). The upper limits are the 3σ limits.

[a] Flux obtained by subtracting the emission of RXJ1131 from the total emission within an aperture.

[b] Flux extracted from the residual map after subtracting a point-source model.

TABLE 2
LENS PARAMETERS CONSTRAINED BY MODELS OF SEVEN VELOCITY CHANNELS

Parameters		Median values
Offset in RA	($''$)	0.004±0.027
Offset in Dec	($''$)	0.003±0.027
Axial Ratio		0.56±0.16
Position Angle	(deg)	103±22
Einstein Radius	($''$)	1.833±0.002

NOTE. — Parameters describing the foreground lens are obtained based on the median in the preliminary models (see text for details). All angular offsets are with respect to $\alpha=11^{\rm h}31^{\rm m}51^{\rm s}.44$, $\delta=-12^{\circ}31'58''.3$ (J2000).

the VLA image as well as the uncertainties provided by previous SIE lens model (C06). We initialize the Einstein Radius based on the model parameters reported by C06 and impose a uniform prior using $\pm3\sigma$ of their uncertainties. The sources are modeled using elliptical Gaussian profiles, which are parameterized by six free parameters: the positional offset in R.A. and Dec. relative to the lens, the intrinsic flux density, the effective radius, the axial ratio, and the position angle. The position of each source is allowed to vary between $\pm1''.5$ (i.e., within the Einstein Radius) and the effective radius is allowed to vary from $0''.01$–$2''$.

Our code uses an Markov Chain Monte Carlo (MCMC) approach to sample the posterior probability distribution function (PDF). In each model, we require a target acceptance rate of ∼0.25–0.5 and check for chain convergence by inspecting trace plots and requiring the samples are beyond at least an autocorrelation time. We thus employ ∼50,000 samples as the initial "burn-in" phase to stabilize the Markov chains (which we then discard) and use the final ∼5,000 steps, sampled by 128 walkers, to identify the posterior. Here, we identify the best-fit model and the quoted uncertainties using the median and the 68% confidence intervals in the marginal PDFs.

We first obtain a preliminary lens model for each channel slice independently, where their lens parameters are allowed to vary and are initialized according to the aforementioned way. We obtain the final model by repeating the modeling over each slice but fixing their lens parameters to the overall median in the preliminary models, as listed in Table 2. This ensures that all models share the same lens profile. The magnification factors in Table 3 are determined by taking the ratio between the image plane flux and the source plane flux of each model.

Our model parameters in Table 2, describing the mass distribution of the lensing galaxy, are consistent (within the uncertainties) with that of the SIE model presented by C06. We find a mass of $M(\theta < \theta_{\rm E}) = (7.47 \pm 0.02) \times 10^{11}\, M_{\odot}$ within the Einstein radius.

5.1.1. *Interpretation of the Source-plane Morphology*

The reconstructed source locations in Figure 6 demonstrate an intrinsic velocity gradient across the source plane, which is indicative of a kinematically-ordered disk-like galaxy. Additional support to the disk conjecture can be found in the double-horned line profile (Figure 1) and the observed (image plane) velocity field (Figure 3). Furthermore, C06 also find that the reconstructed source plane emission in optical-NIR is best-reproduced using a $n=1$ Sersic profile. We thus interpret RXJ1131 to be a disk galaxy.

One other interesting result from our lens model is that a better fit is found for the red-most channel if we add a second source component (see top left panel in Figure 6). This is consistent with previous results reported by Brewer & Lewis (2008, hereafter B08), who find an optically faint companion (component F in their paper) ∼2.4 kpc in projection from the AGN host galaxy in V-band, and C06, who find evidence for an interacting galaxy near RXJ1131. Spatially, the red velocity component of the CO emission also coincides with this component F. It is therefore evident that we detect CO($J=2\rightarrow1$) emission in the companion galaxy.

To quantify the type of merger (major v.s. minor) conventionally with a mass ratio, we decompose the total line flux into two components: one from RXJ1131 and the other from its companion. Since the companion is only detected in the red-most channel, we use the best-fit flux densities and magnification factors obtained from the model of this channel to derive the intrinsic gas mass in the companion. Assuming a brightness temperature ratio of $r_{21} = 1$ and a CO luminosity-to-H_2 mass conversion factor of $\alpha_{\rm CO} = 0.8\,(\rm K\ km\,s^{-1}\ pc^2)^{-1}$, we find a molecular gas mass of $M_{\rm gas} = (1.92 \pm 0.09) \times 10^9\,M_\odot$. For the molecular gas mass in RXJ1131, we derive its intrinsic line flux over the FWZI linewidth using the respective magnification factors listed in Table 3, which to first order takes into account effect of differential lensing. This yields $I_{{\rm CO}(J=2\rightarrow1)} = 2.93 \pm 0.70$ Jy km s^{-1}, where the uncertainty includes those on the magnification factors. Adopting the same brightness temperature ratio and $\alpha_{\rm CO}$ as used for the companion, this corresponds to a gas mass of $M_{\rm gas} = (1.38 \pm 0.33) \times 10^{10}\,M_\odot$, implying a gas mass ratio of $\sim$7:1 between RXJ1131 and its companion. We thus classify the system to be a *"wet-wet" minor merger* according to the classification scheme commonly used in literature.

The spatial resolution of the data in hand is a few arcsec, which implies that despite the high SNR and spectral resolution, this data is insufficient to constrain the intrinsic sizes of the lensed galaxies, and thus the magnification factors may be under-predicted.

5.1.2. *Spatial Extent and Differential Lensing*

In the image plane shown in Figure 2, the redshifted component is cospatial with the Einstein Ring seen in the optical image, with most of its apparent flux originating from the lensed arc in the southeast, whereas the blue component is predominately coming from solely the lensed arc. To further illustrate this, we show the channel maps of 21.5 km s^{-1} width and a spatial spectra map of 1.″5 resolution in Figure 7 and Figure 8, respectively. The figures show that emission is present to the west, peaking toward the lensing arc (black crosses in Figure 7) in the red wing, and shifts to the east with decreasing velocity (blue wing). This is consistent with the source plane positions in our models and is suggestive of an extended CO emitting region.

Similar to previous studies of RXJ1131, where differential lensing across *HST V*-, *I*-, and *H*-band has been detected with a magnification factor decreasing from 10.9 to 7.8 (C06), the highly asymmetric CO($J = 2 \rightarrow 1$) line profile suggests that differential lensing is also non-negligible for CO, causing the redshifted emission to be apparently much brighter than the blueshifted component and the asymmetric line profile. This can be explained by the difference in magnification factor ($\mu_{\rm L}$) which varies from 8.7 to 3.1 across the CO($J = 2 \rightarrow 1$) line (Table 3) and also partly due to a contribution from the companion in the redshifted velocity channels. The variation in $\mu_{\rm L}$ across channels is consistent with the source plane positions relative to the caustics in Figure 6, where the red wing emission mainly originates near the cusp of the caustic and the blue wing emission is located beyond the caustics. In fact, the intrinsic line flux of the redshifted and blueshifted emission in RXJ1131 (after subtracting a contribution from the companion) is $I_{{\rm CO}(J=2\rightarrow1)} = 1.26 \pm 0.23$ Jy km s^{-1} and 1.25 ± 0.23 Jy km s^{-1}, respectively, implying an intrinsically symmetric line profile. This is consistent with the source-plane velocity gradient in our lens model (Figure 6 and Figure 9).

TABLE 3
MAGNIFICATION FACTORS OF VARIOUS KINEMATIC COMPONENTS IN CO($J = 2 \rightarrow 1$)

Velocity Range (km s^{-1})	Source 1 $\mu_{\rm L}$	Source 2 $\mu_{\rm L}$
-366 – -258	3.1 ± 0.9	
-237 – -151	4.3 ± 2.4	
-129 – -43	4.2 ± 0.6	
-21.5 – 65	4.1 ± 0.9	
86 – 172	8.7 ± 2.0	
194 – 280	7.6 ± 1.6	
301 – 388	7.2 ± 5.6	6.7 ± 2.5
weighted average	4.4	
median	5.5	

NOTE. — Velocity is taken from the center of each (native) channel without any binning. Each row corresponds to a channel slice used for lens modeling. Source 1 is RXJ1131 and source 2 is its companion. See text for details.

5.2. *CO($J = 2 \rightarrow 1$) Kinematics*

Fitting a four-parameter double-Gaussian that describes two velocity peaks by a single FWHM to the "intrinsic" CO($J = 2 \rightarrow 1$) line profile of RXJ1131 (after correcting for lensing using the magnification factors for various channels and separating the emission from RXJ1131 and its companion), we find a roughly symmetric double-horned profile with a flux ratio of 1.2 ± 0.4 between the peaks, which are separated by $\Delta v_{\rm sep} = 387 \pm 45$ km s^{-1}, and a FWHM of 220 ± 72 km s^{-1}. If we instead fit with a single-Gaussian, we find a FWHM of 600 ± 160 km s^{-1} for RXJ1131 and 73 ± 43 km s^{-1} for the companion galaxy.

A clear velocity gradient and a high velocity dispersion ($\gtrsim$400 km s^{-1}) near the central region is seen in Figure 3. While beam smearing is inevitably the dominant factor in the observed velocity dispersion at the spatial resolution of this data, the exceedingly high velocity dispersion may hint at potential perturbations from the AGN, or internal turbulence due to interactions with the companion, and/or instability due to the large gas content. Therefore, in this scenario, RXJ1131 is likely a disrupted disk galaxy hosting an optically bright quasar and is in the process of merging.

5.3. *CO($J = 2 \rightarrow 1$) Dynamical Modeling*

Assuming the velocities of the respective channels used in the lens modeling correspond to solely the tangential component of the true velocity vector of a rotating disk (i.e., along the major axis), we extract a one dimensional PV diagram in Figure 9 by slicing across their source plane positions (PA: 121°).

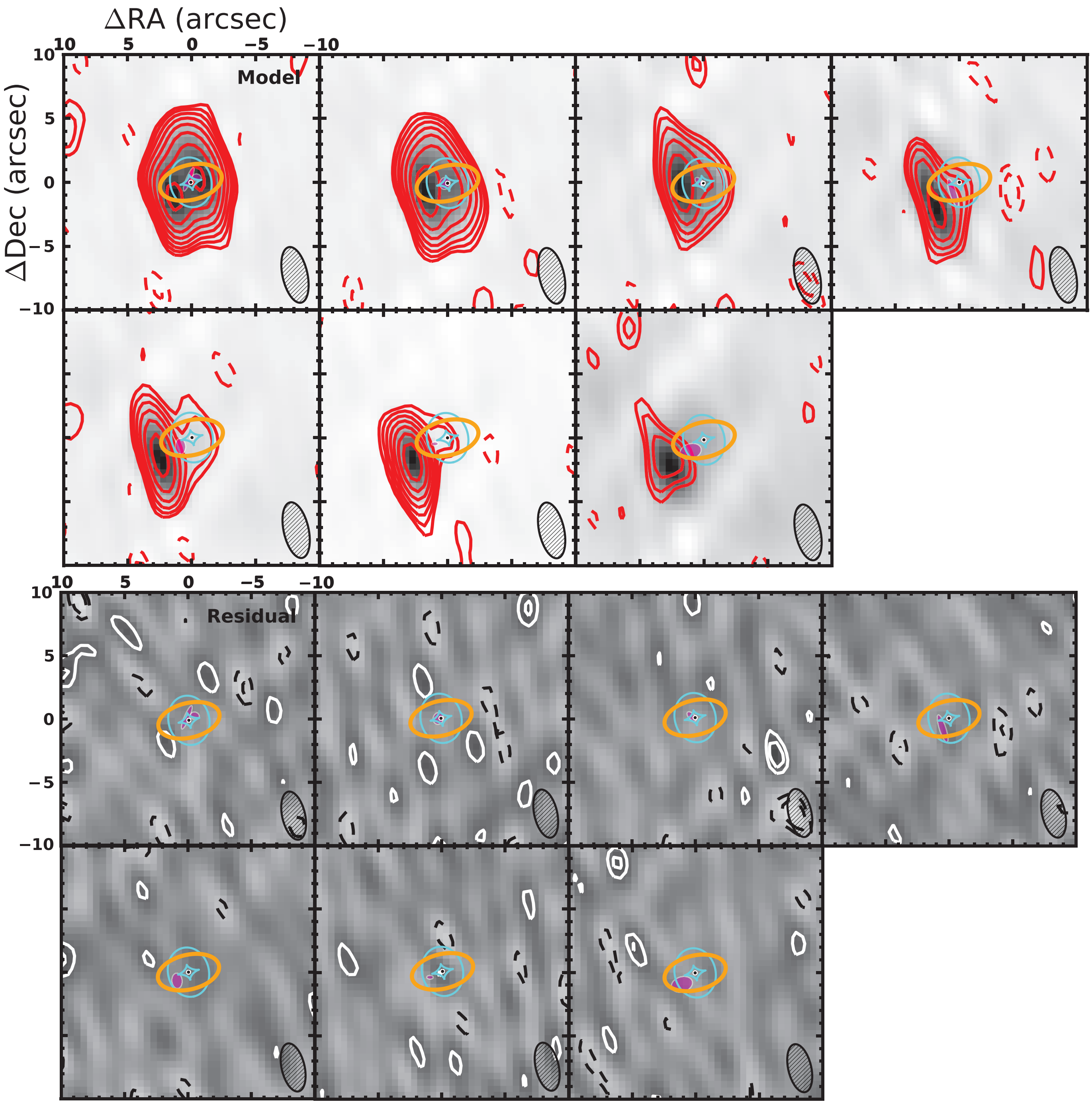

FIG. 6.— Each panel corresponds to a lens model of RXJ1131 performed over a channel slice $\sim$100 km s^{-1} of the CO($J = 2 \rightarrow 1$) data. Top: channel maps of the PdBI CO($J = 2 \rightarrow 1$) emission (red) overlaid on our best-fit lens models (grayscale). The location of the foreground lensing galaxy is indicated by a black dot and its critical curve is traced by the orange solid line. The locations and morphologies (half-light radii) of the reconstructed sources are represented by magenta ellipses. The caustic curves are represented as cyan lines. The beam of the PdBI observations is shown in the bottom right corner of each panel. Bottom: residual images of the best-fit models, obtained by taking the Fourier transform after subtracting the best-fit model from the data in the *uv*-domain. Contours start at $\pm 3\sigma$ and increment at steps of $3 \times 2^n \sigma$, where n is a positive integer.

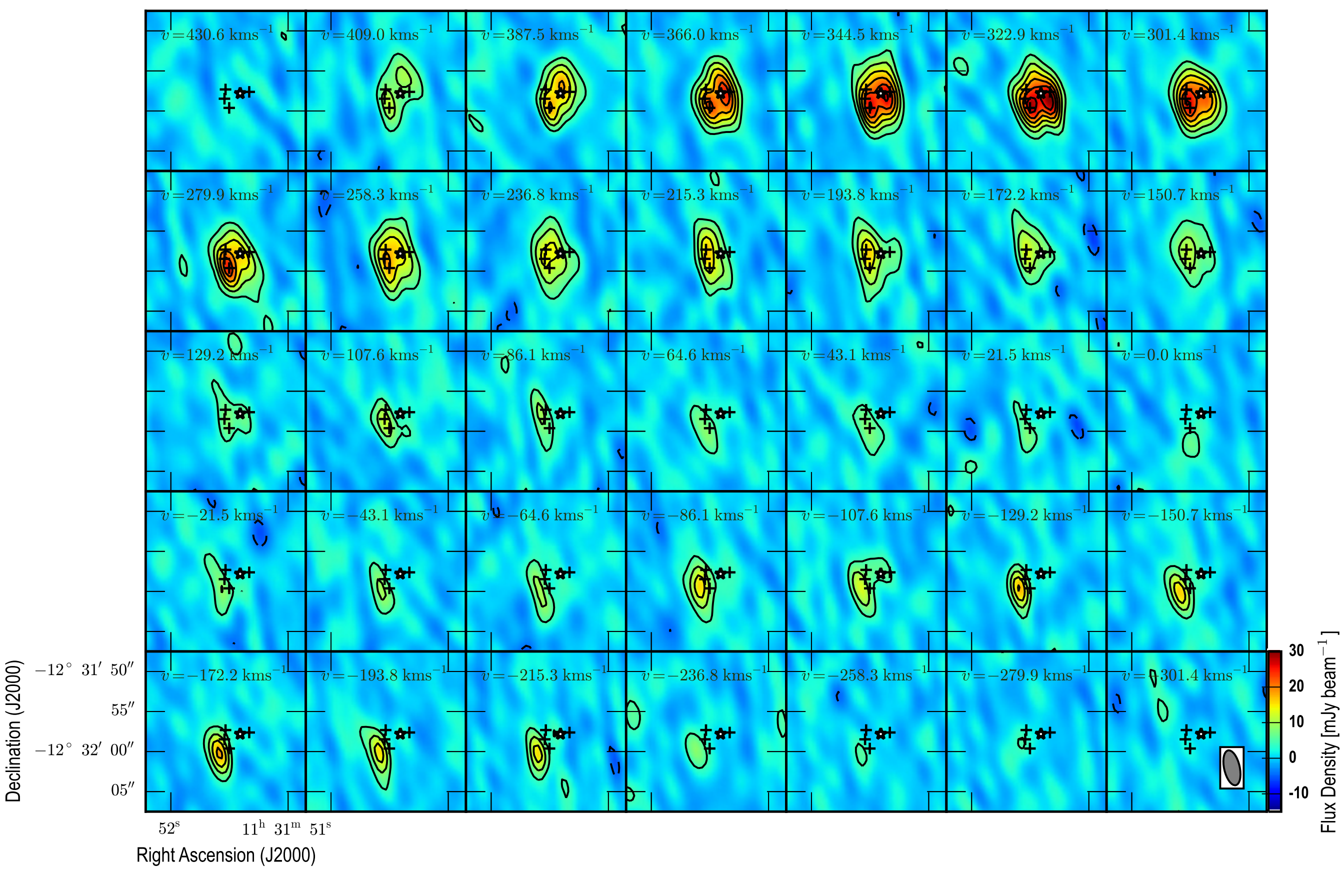

FIG. 7.— Channel maps of the PdBI CO($J=2\rightarrow1$) data cube toward RXJ1131 in 21.5 km s^{-1} resolution. Black crosses indicate the position of the lensed knots (AGN emission, which correspond to components ABCD in C06). The central white-filled star indicates the position of the foreground lensing galaxy (component G in C06). Central velocities are shown at the top of each map. Contours start and increment at steps of $\pm3\sigma$. The beam is denoted in the bottom right panel.

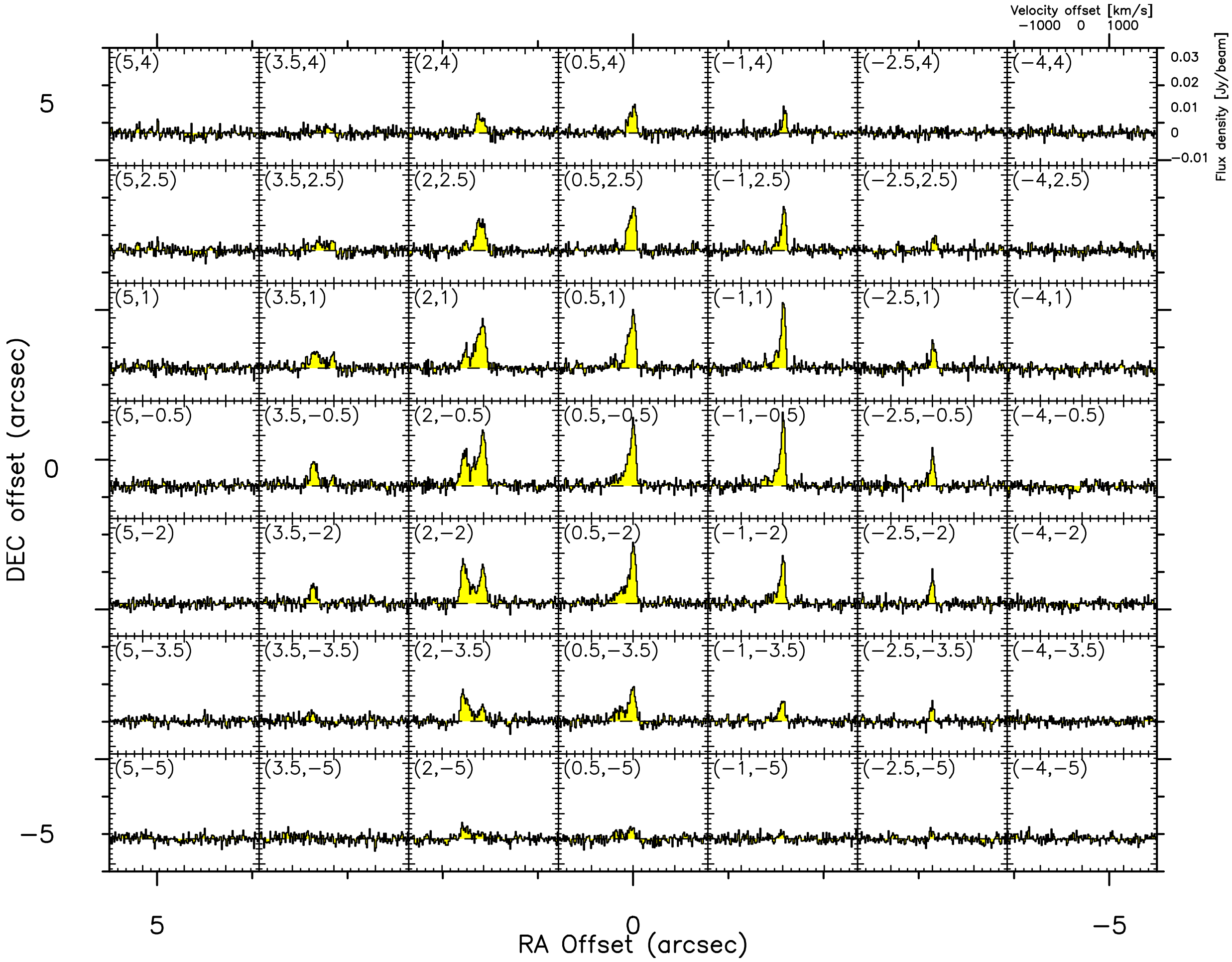

FIG. 8.— CO($J=2\rightarrow1$) spectrum as a function of position, binned by 3 pixels in each direction ($1.''5$). The spectra map covers an extent of $\sim$10"×10" centering on the pixel that corresponds to the lensing galaxy. Spatial offset in arcsec is denoted in top left corner of each panel. The velocity and flux density scales are denoted in the top right panel.

We then attempt to characterize the molecular gas kinematics using an empirically-motivated disk model (e.g., Courteau 1997; Puech et al. 2008; Miller et al. 2011):

$$V = V_0 + \frac{2}{\pi} V_a \arctan(\frac{R}{R_t}), \qquad (1)$$

where V is the observed velocity, V_0 is the velocity at dynamical center, V_a is the asymptotic velocity, and R_t is the "turnover" radius at which the rotation curve becomes flat. We perform non-linear least square fitting using an orthogonal distance regression to find the best-fit parameters, taking into account the uncertainties in both velocity (channel width) and distance offset. We also place an upper limit on R_t <15 kpc to keep this parameter physical (e.g., Puech et al. 2008; Miller et al. 2011). The parameter uncertainties are inferred based on Monte Carlo simulation of 500 iterations, where the input parameters are perturbed according to random Gaussian distributions of sigmas corresponding to their uncertainties. Using this model, we find $V_a = 975 \pm 387$ km s^{-1}, $R_t = 10.7 \pm 5.7$ kpc, and $V_0 = 28 \pm 40$ km s^{-1}. However, since emission is not resolved along the flat regime of the rotation curve, the asymptotic velocity is poorly constrained and the "turnover" radius is at most a lower limit. In particular, V_a and R_t are highly correlated with a Pearson coefficient $R = 0.998$, and 0.027 between V_a and V_0.

The asymptotic velocity (V_a) – an extrapolation of the model out to radius beyond the disk scale-length and half-light radius – is not equivalent to maximum observed velocity ($V_{\rm max}$), which is commonly used in literature to parameterize disc rotation. The arctangent model is most commonly used in studies of the Tully-Fisher relation, where an extrapolation to $V_{2.2}$ (velocity at 2.2 disc scale-length or $\sim$1.375 half-light radius, or $\sim 0.7 R_{\rm opt}$[4]) is typically adopted as the rotation velocity ($V_{\rm max}$ in their terminology) since this corresponds to the radius at which the velocity of a pure exponential disk peaks (Courteau & Rix 1997). We here adopt the maximum *observed* velocity $V_{\rm rot} = 345 \pm 55$ km s^{-1} at 6 ± 3 kpc from the dynamical center as a proxy to the rotation velocity. This radius corresponds to $\sim 0.6 R_e$, where R_e is the half-light radius $\sim$10.3 kpc inferred from the *HST* *I*-band lens model (C06; converted to our cosmology). We note that the source plane half-light radius varies substantially with wavelength. In particular, the half-light radius is found to be $\sim$4 kpc and $\sim$7 kpc in V-band (B08) and H-band (C06), respectively. The CO gas is thus of similar spatial

[4] Radius enclosing 83% of the light distribution.

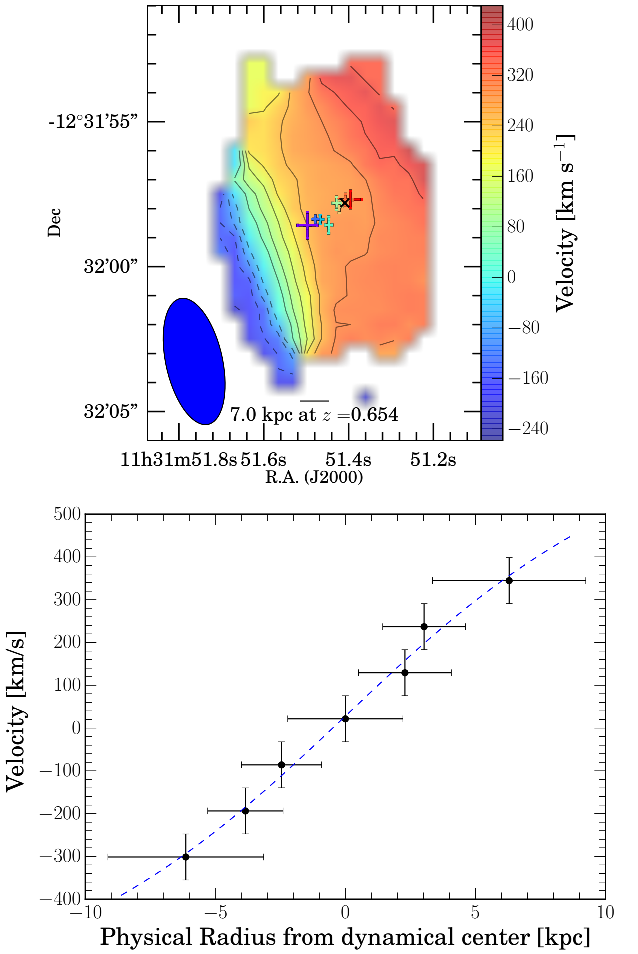

FIG. 9.— Top: Source-plane positions from best-fit CO($J=2\rightarrow1$) lens models are indicated with their associated uncertainties atop the observed first moment map. The contours are at steps of $50\,\mathrm{km\,s^{-1}}$. Bottom: PV slice along the major axis in the source plane at PA = 121°. Dashed line shows the best-fit rotation curve using an arctangent model. The vertical error bars show the channel width for each model and the horizontal error bars are the 1σ uncertainties on the source plane positions.

extents as in H and I-bands.

In the rest-frame, emission in the observed H-band corresponds to NIR emission, tracing radiation from the accretion disk surrounding the central AGN and also from old and evolved stellar populations; I-band corresponds to roughly the optical V-band, tracing stellar radiation from existing, less massive (i.e., longer-lasting) stars; V-band corresponds to roughly U-band, tracing radiation from massive young stars in the host galaxy. Hence, the V-band compactness may be explained in part due to the fact that its emission is more susceptible to dust extinction than in other bands and/or a central starburst caused by higher concentrations of star-forming gas towards the central regions – owing to gravitational perturbations induced from interactions with the companion (e.g., Di Matteo et al. 2005). This is consistent with the picture that old stars form first and constitute the bulge component of a spiral galaxy and that nuclear starbursts (in the inner few kpc) can be triggered latter in mergers.

5.4. *SED Modeling*

TABLE 4
SED FITTING RESULTS

Parameters		With 24μm	Without 24μm
T_d	(K)	$52.0^{+4.0}_{-4.1}$	$58.2^{+14.5}_{-14.4}$
β		$1.8^{+0.5}_{-0.6}$	$2.1^{+0.3}_{-0.3}$
α		$1.6^{+0.5}_{-0.5}$	$8.9^{+6.9}_{-6.3}$
λ_0 [a]	(μm)	548^{+285}_{-307}	367^{+125}_{-145}
$\lambda_{\rm peak}$ [b]	(μm)	162^{+16}_{-30}	146^{+39}_{-44}
$f_{\rm norm,\,500\mu m}$ [c]	(mJy)	59^{+14}_{-13}	60^{+5}_{-5}
$L_{\rm FIR}$ [d]	($10^{12}\,L_\odot$)	$3.81^{+2.04}_{-1.92}$	$4.72^{+2.54}_{-2.26}$
M_d [e]	($10^8\,M_\odot$)	22^{+5}_{-18}	11^{+5}_{-6}

NOTE. — Errors reported here are $\pm1\sigma$. $L_{\rm FIR}$ and $M_{\rm d}$ are not corrected for lensing.
[a] Observed-frame wavelength where $\tau_\nu = 1$
[b] Observed-frame wavelength of the SED peak
[c] Observed-frame flux density at 500 μm
[d] Rest-frame 42.5–122.5 μm luminosity
[e] Derived assuming absorption mass coefficient of κ=2.64 m^2 kg^{-1} at λ = 125.0 μm (Dunne et al. 2003)

We fit dust SED models to the 24 μm–2.2 mm photometry in Figure 10, where we also include the IRAS 60 μm and 100 μm upper limits to constrain the dust peak. The fit is performed with the code MBB_EMCEE (e.g., Riechers et al. 2013; Dowell et al. 2014), which samples the posterior using an MCMC approach and uses instrumental response curves to perform color correction on-the-fly. The SED model consists of a modified-blackbody function with a power-law attached to the Wien side to account for an excess in the MIR owing to warm, small dust emission. The model is thus described by five free parameters: the rest-frame characteristic dust temperature (T_d), the emissivity index (β), the power-law index (α), the flux normalization at 500 μm ($f_{\rm norm}$), and the observed-frame wavelength at which the emission becomes optically thick (λ_0). We impose an upper limit of 100 K on T_d (see e.g., Sajina et al. 2012), a Gaussian prior centered around $\mu = 1.9$ with $\sigma = 0.3$ on β, and an upper limit of 1000 μm on λ_0. We check for chain convergence by requiring the autocorrelation length of each parameter to be less than the number of steps taken for the burn-in phase (which are then discarded). Here we report the statistical means and the 1σ confidence interval in the marginal PDFs as the best-fit parameters, as listed in Table 4.

In the first model, we include the 24 μm data to constrain the power-law index. Based on the best-fit of this model, we find a far-IR luminosity (rest-frame $42.5-122.5\,\mu$m) of $3.81^{+2.04}_{-1.92}\times10^{12}\,L_\odot$ and a dust mass of $22^{+5}_{-18}\times10^8\,M_\odot$, uncorrected for lensing. For the mass absorption coefficient, we adopt $\kappa = 2.64\,\mathrm{m^2kg^{-1}}$ at 125.0 μm (rest frame; Dunne et al. 2003). The dust mass uncertainty does not include those in the absorption coefficient.

A fit including the MIR 24 μm photometry is likely an upper limit on the far-IR luminosity arising from the starburst in the AGN host galaxy. If we instead fit for a model excluding the 24 μm constraint, two major consequences are immediately apparent. First, the power-law index is poorly-constrained (see Table 4). Second, the steep power-law implies a small contribution from the power-law regime to the total IR luminosity as compared to the graybody. Thus, the far-IR luminosity in this model should, in principle, correspond to a lower limit on the cold dust emission. Using the best-fit parameters for this model, we find a total IR luminosity $L_{\rm IR}$ (rest-frame $8-1000\,\mu$m) of $9.71^{+6.14}_{-6.05}\times10^{12}\,L_\odot$, a far-IR luminosity $L_{\rm FIR}$ of $4.72^{+2.54}_{-2.26}\times10^{12}\,L_\odot$ and a dust mass $M_{\rm dust}$ of $11^{+5}_{-6}\times10^{8}\,M_\odot$, uncorrected for lensing. Taken at face value, this implies a FIR-to-IR luminosity ratio of $\sim$58 $\pm$ 35%.

The dust temperature from both models is similar to that of ULIRGs at $0.6 < z < 1.0$ (54 ± 5 K; Combes et al. 2013, hereafter C13). We note the far-IR luminosity is comparable in both models, which is not surprising given the lack of constraints in the MIR. For the subsequent analysis, we adopt the physical quantities from the first model (i.e., with constraints at 24 μm). The choice of SED model does not affect the derived star formation rate (SFR) given the similar far-IR luminosity. Yet, the dust mass is higher in the former but consistent within the uncertainties. We correct for lensing using the median magnification factor ($\mu_{\rm L}$ = 5.5) from the CO lens models. This yields a $L_{\rm FIR}$ of $(6.9\pm3.6)\times10^{11}\,L_\odot$ and a total IR luminosity of $\sim1.5\times10^{12}\,L_\odot$, implying RXJ1131 is a ULIRG. Assuming a Salpeter initial mass function (Salpeter 1955), we find a SFR$_{\rm FIR}$ of $120\pm63\,M_\odot$ yr^{-1} using the standard conversion (Kennicutt 1998).

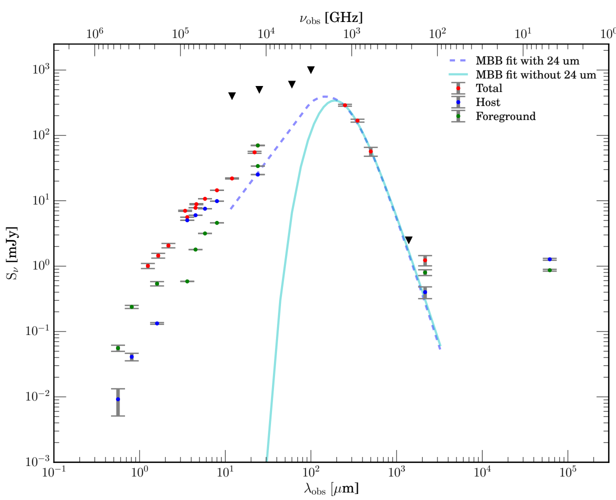

FIG. 10.— SEDs of RXJ1131 and its lensing galaxy. The photometry is listed in Table 1. Best-fit SED models of the thermal dust emission towards RXJ1131 with(out) MIR constraint at 24 μm are plotted as dashed (solid) lines.

5.5. *ISM Properties*

In this section, we derive the gas properties of the merger system based on CO($J=2\rightarrow1$) and compare with those reported by C13, which is the largest sample of IR-luminous galaxy at similar redshift ($0.6 < z < 1.0$) with CO measurements[5]. We note that their results are based on CO($J=2\rightarrow1$) and CO($J=4\rightarrow3$) line observations with the IRAM 30-m single-dish telescope.

5.5.1. *Linewidth and Sizes*

A linewidth of $\Delta v_{\rm FWHM}\sim600\pm160\,{\rm km\,s^{-1}}$ found from fitting a single Gaussian is considerably larger that those in the (C13) sample ($370\,{\rm km\,s^{-1}}$) as well as local ULIRGs ($300\pm85\,{\rm km\,s^{-1}}$, with the largest being $480\,{\rm km\,s^{-1}}$; Solomon et al. 1997, hereafter S97). Yet, given the dynamic nature of these galaxies, a CO linewidth of $\sim$600 may not be surprising. Indeed, a linewidth of Δv = 750 km s^{-1} has been observed in a local LIRG (Arp 118) (Solomon & Vanden Bout 2005). Such FWHM is also commonly observed in high-z starburst galaxies ($780\pm320\,{\rm km\,s^{-1}}$; e.g., Greve et al. 2005).

The CO gas in RXJ1131 is $\sim6\pm3$ kpc in radius (in the source plane), which is more extended than the sample of disk-like U/LIRGs studied by Ueda et al. (2014, hereafter U14), who find an average radius of 3.5 ± 2.3 kpc but with a range of $1.1-9.3$ kpc. Such a range is consistent with the results reported by Gao & Solomon (1999), where they also find CO disks extending out to $R\sim10$ kpc. In contrast to the results reported in the classical study by Downes & Solomon (1998, hereafter DS98), who find molecular gas sizes of $R<1$ kpc in their sample of local ULIRGs (see also Bryant & Scoville 1999 and Iono et al. 2009), it appears that the molecular gas in ULIRGs can be distributed over large regions comparable to those reported in high-z ($z>1$) galaxies ($R\sim7$ kpc; G05; Daddi et al. 2010; Riechers et al. 2011; Ivison et al. 2011). While we cannot draw any conclusions on the evolution of molecular gas size as we are only studying one ULIRG at intermediate redshift, it appears that local ULIRGs are composed of mergers at various stages of merging, and are therefore not necessarily more compact than high-z SMGs (cf. e.g., Iono et al. 2009).

We do not attempt to derive a SFR surface density and gas surface density since we do not have any constraints on the dust continuum size and the fact that the gas surface density is unlikely to be constant across the CO region given the centrally concentrated V-band emission, which we interpret as merger-induced starburst (see §5.1.1). Should we decide to do this, it would imply a series of assumptions to be made, leading to surface densities that are not meaningful in any case.

5.5.2. *Dynamical Mass*

Assuming the gas is virialized, the dynamical mass can be approximate as $M_{\rm dyn} = \sigma^2 R/G$, where σ is the velocity dispersion, or the rotational velocity in the case of a rotating disk model (i.e., $\sigma = V_{\rm rot}\sin i$). Using a rotational velocity $V_{\rm rot}\sin i = 345\,{\rm km\,s^{-1}}$ (see §5.3), we find a dynamical mass of $M_{\rm dyn}\sin^2 i\,(<6\,{\rm kpc}) = 17\times10^{10}\,M_\odot$ enclosed within the CO-emitting region in RXJ1131. If we instead consider the CO($J=2\rightarrow1$) line peak separation ($\Delta v_{\rm sep}/2\sim200\,{\rm km\,s^{-1}}$) as the rotation velocity, we

[5] The far-IR luminosity in C13 is derived based on 60 μm and 100 μm IRAS fluxes, and using a different definition of $L_{\rm FIR}$: rest-frame $40-500\,\mu$m. Following this convention, we find a far-IR luminosity of $L_{\rm FIR}$ = $(8.8\pm0.4)\times10^{11}(\mu_{\rm L}/5.5)^{-1}\,L_\odot$ and a SFR of $(150\pm70)\,M_\odot$ yr^{-1}.

find $M_{\rm dyn}\sin^2 i\,(<6\,{\rm kpc}) = 5.8\times10^{10}\,M_\odot$. We correct for the inclination effect using the morphological axial ratio ($a/b \sim 1\farcs8$ / $3\farcs25$) from the reconstructed image (Figure 3 in C06), yielding an inclination angle of 56.4°, which is consistent with the observed unobscured AGN and an observable double peak line profile. The dynamical mass is then $8.3\times10^{10}M_\odot < M_{\rm dyn} < 25\times10^{10}M_\odot$. Our estimate should be considered at best an upper limit since the gas is unlikely to be virialized in RXJ1131. For the following sections, we use the lower limit $(8.3\pm1.9)\times10^{10}\,M_\odot$ as the dynamical mass as it is derived in a manner similar to commonly used in literature (e.g., S97; DS98; G05).

Using the velocity dispersion obtained with a single Gaussian fit to the line profile of the companion (σ = 30 km s^{-1}) and its intrinsic source size of ∼700 pc obtained from the *HST V*-band lens model (B08), we find a dynamical mass of $M_{\rm dyn}\sin^2 i = 5\times10^6\,M_\odot$. This corresponds to $M_{\rm dyn} = 2\times10^7\,M_\odot$ if we assume an inclination angle of 30°. We note that this is substantially lower than its gas mass, which is a more reliable estimate based on the data in hand. We adopt the V-band size as the radius R owing to the fact that it is the only size estimate available for the companion. We do not use this dynamical mass for deriving any additional physical parameters, and thus it does not alter our interpretations of the system throughout this paper.

5.5.3. *Gas Mass and Gas Ratios*

A total molecular gas mass of $M_{\rm gas}^{\rm total}$ = $(1.57\pm0.38)\times10^{10}\,M_\odot$ is residing within the merger system (see §5.1.1). This is comparable to those found in the C13 sample as well as local U/LIRGs (Sanders & Mirabel 1996, S97) but higher than in local LIRGs (U14), as expected. Our finding is thus consistent with previous results, where high-z galaxies tend to have higher molecular gas mass and is distributed over larger spatial extents (e.g., SV05; R11; I11). Using the dynamical mass and the total gas mass ($M_{\rm gas}^{\rm total}$), we find a gas mass fraction of $f_{\rm gas-dyn}$ = 0.19 ± 0.37, which is consistent with the results reported by C13: a gas fraction of 15% in ULIRGs at $0.2<z<0.4$ and 24% in those at $0.6<z<1.0$, and those from resolved measurements of local ULIRGs (DS98). This implies that the gas fraction in ULIRGs at $z<1$ is similar to those in high-z "normal" star-forming disc galaxies (assuming an $\alpha_{\rm CO}$ conversion factor of 0.8 (K km s^{-1} pc^2)$^{-1}$; Daddi et al. 2010; Tacconi et al. 2010) as well as high-z starburst galaxies (Bothwell et al. 2013, with similar CO sizes between the two populations (see §5.5.1); cf. smaller CO sizes from earlier studies; DS98).

Using the lensing-corrected dust mass, we find a gas-to-dust ratio of 40 ± 34, which is significantly lower than the statistical average of $f_{\rm gas-dust} = 206$ in the C13 sample but consistent with their range of values and the Wilson et al. (2008) sample of local ULIRGs. We note that the gas-to-dust ratio maybe biased low as the optically thick gas is likely to be more extended than the dust, leading to an overall lower magnification factor than the dust emission, and thus an overestimate of the dust mass via our adoption of the CO magnification factor.

There are a number of systematic uncertainties associated with this quantity, e.g., the mass opacity coefficient κ, the $\alpha_{\rm CO}$ conversion factor, and the brightness temperature ratio R_{21}. The fact that RXJ1131 has a lower dust-to-gas ratio and appears to be more dusty than most ULIRGs at the same epoch may imply different physical environment compared to others. If we instead use the "Galactic" $\alpha_{\rm CO}$ value, the gas mass (and thus gas-to-dust ratio) would be ∼6 times higher. On the other hand, we would also obtain a higher gas mass if we assume subthermal excitation between CO($J=2\rightarrow1$) and CO($J=1\rightarrow0$) line emission. However, we expect this to be a minor effect as ULIRGs are observed to be thermalized up to J = 3 or 4.

5.5.4. *SFE and Depletion Timescales*

To first order, the star formation efficiency (SFE = $L_{\rm FIR}$ $/M_{\rm gas}$) indicates the star formation rate per unit solar mass of molecular gas available in a galaxy. Using a wavelength range of $40-500\,\mu$m defined in C13 as the far-IR luminosity, we find an SFE of 58 ± 10 $L_\odot$ $M_\odot^{-1}$, which is on the low end among other U/LIRGs (Solomon et al. 1997; Combes et al. 2011) but similar to those of low-z spiral galaxies ($z<0.1$; SV05). In constrast, a star formation efficiency of $>$100 $L_\odot$ $M_\odot^{-1}$ has been reported in ULIRGs and SMGs at $0.6<z<3$ (Tacconi et al. 2008, R11; C13). Assuming the star formation continues at the current rate without gas replenishment and is the only way to consume the gas reservoir, this corresponds to a depletion time of $\tau = 102\pm25$ Myr. Since the star formation rate is expected to vary in an interacting system and that AGN accretion also consumes some fraction of the gas, the depletion timescale should only be considered as an upper limit.

The SFE (using the above definition) is highly dependent on the gas mass. Yet, the use of an "ULIRG" $\alpha_{\rm CO}$ value is not well justified and should only be considered as a lower limit (see S97). It may be more appropriate to use an $\alpha_{\rm CO}$ closer to the "Galactic" value in some ULIRGs (e.g., Papadopoulos et al. 2012). From numerical models, it is found that mergers on average have lower $\alpha_{\rm CO}$ values than disk galaxies (Narayanan et al. 2012). But since the gas temperatures and velocity dispersions in minor mergers do not deviate from galactic GMCs as much as in major mergers, the $\alpha_{\rm CO}$ may not be as extreme as 0.8 (K km s^{-1} pc^2)$^{-1}$. Hence, we can derive an upper limit on the gas mass for RXJ1131 using the Galactic value of 4.6 (K km s^{-1} pc^2)$^{-1}$. This yields a gas mass (and thus a SFE) that is ∼6 times higher. In contrast to results in the classical study of nearby ULIRGs by DS98, who find that the gas mass exceeds the dynamical mass using the Galactic conversion factor (and thus inappropriate for their sample), the gas mass derived for RXJ1131 using the Galactic value is consistent with its dynamical mass.

Alternatively, the relatively low SFE maybe intrinsic to RXJ1131. In that case, RXJ1131 may evolve into a disc galaxy with a small bulge component in the context of theoretical simulations by Hopkins et al. (2009), who suggest that the disc component in a gas-rich progenitor galaxy can survive post-merging by lowering the star formation efficiency (and thus less efficient at removing the angular momentum of the gas), thereby enabling a higher gas fraction to be retained and distributed over a larger extent.

6. DISCUSSION

6.1. *Velocity Offset and a Recoiling Black Hole*

Using the redshift deduced from the CO line as the systemic redshift, we find a velocity offset of $\sim$780 km s^{-1} with the optical lines: the broad Mg II 2798Å and the narrow [O III] 4959, 5007Å lines ($z_{\rm AGN}$ = 0.658; Sluse et al. 2003). This indicates that the broad line region (BLR) of the AGN is at a slightly higher redshift than the host galaxy. From the CO renzogram and channel maps in Figure 2 and Figure 7, the emission corresponding to the the line center are not co-spatial with the optical quasar. In particular, the quasar emission forms the point-like images along the lensing arc, which is spatially offset to the NW of the CO line center emission. Spatial offsets between optical BLRs and CO emission are not uncommon but such a high kinematic offset is not commonly observed. For instance, the velocity offset between AGNs and their hosts galaxies in an SDSS sample of ongoing mergers at $z < 0.21$ is at most $\sim$410 km/s (Comerford & Greene 2014). The same authors also suggest mechanisms such as AGN outflows, jets, and gravitational recoil of SMBHs in post-merger as plausible explanations for these offsets.

AGN outflows or starburst-driven winds have been observed in e.g., SMMJ1636+4057 (Swinbank et al. 2005), but no evidence for outflows are found in RXJ1131 in the existing data. Alternatively, it can be an indication of the BH(s) orbiting the a common center in the host galaxy. In principle, this would only be valid if the velocity offset between the BLR and the narrow line of the gas in the host galaxy is consistent with its orbital velocity. Since Sluse et al. (2003) only report a redshift combining the broad and narrow lines, the lack of a redshift from solely the BLR of the AGN precludes us from interpreting this as the favoured explanation for the velocity offset.

In fact, a large velocity offset can also result from a recoiling black hole (BH) where its BLR is moving at high velocity relative to the bulk of the host galaxy and the ionized gas (Madau & Quataert 2004; Bonning et al. 2007; Loeb 2007). Such a scenario may occur after galaxies and their BHs merge, during which their orbital energy is being released as gravitational wave to overcome the last stable orbit. This results in a recoil in the merged BH for an uneven BH mass merger as a non-zero net angular momentum is also being carried away. Depending on their initial conditions, numerical relativity simulations have shown that the recoil velocity can reach up to $\sim$4000 km s^{-1} for spinning BHs (e.g., Campanelli et al. 2007). This together with the fact that the BH in RXJ1131 has a high spin parameter (Reis et al. 2014) renders the recoiling BH scenario a viable option for the origin of the optical velocity offset. To reconcile this picture with the fact that a companion is still observed, the system may be in its subsequent stages of (minor) merging but was initially a major merger. This would imply previous encounters between RXJ1131 and its companion, which would also explain the spinning BH.

It is worth noting that while these large velocity offsets are theoretically achievable, they are not commonly observed — only a few objects have been reported with optical offsets $\gtrsim$1000 km s^{-1}. For instance, the most promising candidate of a recoiling BH with both spectroscopy and imaging signatures is CID-42 at $z = 0.359$, which has a velocity offset of $\sim$1300 km s^{-1} between the narrow and broad component of Hβ (Civano et al. 2010). Other examples include the type-1 QSO SDSS 0956+5127 at $z \sim 0.714$, with an offset of 1200 km s^{-1} between Mg II 2798Å and [O III] 4959, 5007Å lines (Steinhardt et al. 2012), and SDSSJ0927+2943 at $z \sim 0.713$, with an offset of 2650 km s^{-1} (Komossa et al. 2008).

6.2. *Merger stage RXJ1131-1231*

The (gas) mass ratio, the intrinsic CO line profile, and the source-plane velocity field are all evident of a minor merger, in good agreement with an earlier study by B08 who independently conclude the presence of a dwarf companion of size $\sim$700 kpc across. Since minor mergers may in some cases result from previous passage of major mergers, it is possible that RXJ1131 has encountered with the progenitor galaxy of the companion and is undergoing the subsequent series of minor merging. One piece of evidence comes from the compact UV emission, which can be starburst resulting from gas accumulation owing to a non-axisymmetric perturbation from the companion. The highly spinning black hole in RXJ1131 is also consistent with this hypothesis. If we favor the gravitational wave recoil mechanism to explain the optical velocity offset, it would also imply the black holes (and their host galaxies) have merged or are at their final coalescence. In addition, the source-plane CO position of the companion appears to be consistent with a picture where its molecular gas is mixed with RXJ1131 (but with large uncertainties). The IR luminosity also agrees with the results from previous studies: AGNs are typically found in late stage mergers (Yuan et al. 2010; Iwasawa et al. 2011; Carpineti et al. 2012) and only major mergers near their final coalescence can provide $L_{\rm IR} > 10^{12} L_\odot$, (e.g., Carpineti et al. 2015; Larson et al. 2016).

It may be puzzling as to why the stellar emission in the companion is spatially offset from RXJ1131 while its CO gas appears to be mixed-in if they have encountered. This phenomenon is in fact not unique to our source. The gas cores of the individual mergers NGC 6090 and NGC 6240 are also observed to be coalescing while their stellar cores remain separated (0.5–3 kpc; Bryant & Scoville 1999). Although this is difficult to reconcile with the fact that the stellar light in the companion originates from recent star formation (UV emission). More sensitive and higher resolution observations will be needed to confirm any offsets between the CO gas and the stellar light in the companion. Another puzzle may be the absence of morphological features. One straightforward explanation may simply be the lack of spatial resolution. Alternatively, it may be a result of the offset in timing between observable morphological disturbances and the merger-induced starbursts (Lotz et al. 2008).

6.3. *Fate of RXJ1131*

The classical picture for mergers is one where they are responsible for the formation of the local red and passive spheroidal galaxies. With more realistic treatments of star formation and feedbacks in recent simulations, it has been suggested that it is possible to suppress bulge formation in gas-rich mergers, thereby evolving into large disks (Springel & Hernquist 2005; Robertson et al. 2006; Hopkins et al. 2009). Since both RXJ1131 and its companion are gas-rich and that the bulk of the angular momentum of the gas is retained in minor mergers, it is likely that RXJ1131 will evolve into either a "normal" elliptical/S0 galaxy or a large disk galaxy. In the latter, the stellar populations from the companion will be displaced onto the dominant galaxy to thicken the disk (e.g., Lotz et al. 2008; Robertson et al. 2006). Given that the molecular gas in RXJ1131 is distributed in an extended disk configuration and that its SFE is on the low end among other ULIRGs, it is more conceivable that RXJ1131 will evolve into the latter. Other mechanisms e.g. formation of bar-like structures will be needed to remove the angular momentum of the gas more efficiently to transform the gas disc into a stellar spheroid and AGN feedbacks are also necessary to halt further activities for RXJ1131 to evolve into an E/S0 galaxy (Lotz et al. 2008).

This work is based on observations carried out under project number S14BX001 with the IRAM NOEMA Interferometer. IRAM is supported by INSU/CNRS (France), MPG (Germany) and IGN (Spain). Support for CARMA construction was derived from the Gordon and Betty Moore Foundation, the Kenneth T. and Eileen L. Norris Foundation, the James S. McDonnell Foundation, the Associates of the California Institute of Technology, the University of Chicago, the states of Illinois, California, and Maryland, and the National Science Foundation. Ongoing CARMA development and operations are supported by the National Science Foundation under a cooperative agreement and by the CARMA consortium universities. The National Radio Astronomy Observatory is a facility of the National Science Foundation operated under cooperative agreement by Associated Universities, Inc. This research made use of data obtained with *Herschel*, an ESA space observatory with science instruments provided by European-led Principal Investigator consortia and with important participation from NASA. This research has made use of NASA's Astrophysics Data System Bibliographic Services. This work is based in part on observations made with the *Spitzer Space Telescope*, which is operated by the Jet Propulsion Laboratory, California Institute of Technology under a contract with NASA. This publication made use of data products from the Wide-field Infrared Survey Explorer, which is a joint project of the University of California, Los Angeles, and the Jet Propulsion Laboratory/California Institute of Technology, funded by the National Aeronautics and Space Administration. This publication made use of data products from the Two Micron All Sky Survey, which is a joint project of the University of Massachusetts and the Infrared Processing and Analysis Center/California Institute of Technology, funded by the National Aeronautics and Space Administration and the National Science Foundation. This research made use of the NASA/IPAC Extragalactic Database (NED) which is operated by the Jet Propulsion Laboratory, California Institute of Technology, under contract with the National Aeronautics and Space Administration. This research made use of Astropy, a community-developed core Python package for Astronomy (Astropy Collaboration et al. 2013). This research made use of APLpy, an open-source plotting package for Python hosted at `http://aplpy.github.com`.

Facilities: IRAM PdBI, CARMA, VLA, Herschel(SPIRE), WISE, IRAS, 2MASS, Spitzer(IRAC, MIPS), HST(ACS, NICMOS)

Astropy Collaboration, Robitaille, T. P., Tollerud, E. J., et al. 2013, A&A, 558, A33
Bonning, E. W., Shields, G. A., & Salviander, S. 2007, ApJ, 666, L13
Bothwell, M. S., Smail, I., Chapman, S. C., et al. 2013, MNRAS, 429, 3047
Brewer, B. J., & Lewis, G. F. 2008, MNRAS, 390, 39
Bryant, P. M., & Scoville, N. Z. 1999, AJ, 117, 2632
Bussmann, R. S., Riechers, D., Fialkov, A., et al. 2015, ApJ, 812, 43
Bussmann, S., Leung, T. K. D., & Conley, A. 2015, uvmcmcfit
Campanelli, M., Lousto, C. O., Zlochower, Y., & Merritt, D. 2007, Physical Review Letters, 98, 231102
Carpineti, A., Kaviraj, S., Darg, D., et al. 2012, MNRAS, 420, 2139
Carpineti, A., Kaviraj, S., Hyde, A. K., et al. 2015, A&A, 577, A119
Civano, F., Elvis, M., Lanzuisi, G., et al. 2010, ApJ, 717, 209
Claeskens, J.-F., Sluse, D., Riaud, P., & Surdej, J. 2006, A&A, 451, 865
Combes, F., García-Burillo, S., Braine, J., et al. 2011, A&A, 528, A124
—. 2013, A&A, 550, A41
Comerford, J. M., & Greene, J. E. 2014, ApJ, 789, 112
Courteau, S. 1997, AJ, 114, 2402
Courteau, S., & Rix, H.-W. 1997, in Bulletin of the American Astronomical Society, Vol. 29, American Astronomical Society Meeting Abstracts, 1332
Daddi, E., Bournaud, F., Walter, F., et al. 2010, ApJ, 713, 686
Di Matteo, T., Springel, V., & Hernquist, L. 2005, Nature, 433, 604
Dowell, C. D., Conley, A., Glenn, J., et al. 2014, ApJ, 780, 75
Downes, D., & Solomon, P. M. 1998, ApJ, 507, 615
Dunne, L., Eales, S. A., & Edmunds, M. G. 2003, MNRAS, 341, 589
Fazio, G. G., Hora, J. L., Allen, L. E., et al. 2004, ApJS, 154, 10
Gao, Y., & Solomon, P. M. 1999, ApJ, 512, L99
Greve, T. R., Bertoldi, F., Smail, I., et al. 2005, MNRAS, 359, 1165
Hinshaw, G., Larson, D., Komatsu, E., et al. 2013, ApJS, 208, 19
Hopkins, P. F., Cox, T. J., Younger, J. D., & Hernquist, L. 2009, ApJ, 691, 1168

Iono, D., Wilson, C. D., Yun, M. S., et al. 2009, ApJ, 695, 1537
Ivison, R. J., Papadopoulos, P. P., Smail, I., et al. 2011, MNRAS, 412, 1913
Iwasawa, K., Sanders, D. B., Teng, S. H., et al. 2011, A&A, 529, A106
Kennicutt, Jr., R. C. 1998, ARA&A, 36, 189
Komossa, S., Zhou, H., & Lu, H. 2008, ApJ, 678, L81
Larson, K. L., Sanders, D. B., Barnes, J. E., et al. 2016, ArXiv e-prints, arXiv:1605.05417
Loeb, A. 2007, Physical Review Letters, 99, 041103
Lotz, J. M., Jonsson, P., Cox, T. J., & Primack, J. R. 2008, MNRAS, 391, 1137
Madau, P., & Quataert, E. 2004, ApJ, 606, L17
Miller, S. H., Bundy, K., Sullivan, M., Ellis, R. S., & Treu, T. 2011, ApJ, 741, 115
Narayanan, D., Krumholz, M. R., Ostriker, E. C., & Hernquist, L. 2012, MNRAS, 421, 3127
Neugebauer, G., Habing, H. J., van Duinen, R., et al. 1984, ApJ, 278, L1
Ott, S. 2010, in Astronomical Society of the Pacific Conference Series, Vol. 434, Astronomical Data Analysis Software and Systems XIX, ed. Y. Mizumoto, K.-I. Morita, & M. Ohishi, 139
Papadopoulos, P. P., van der Werf, P., Xilouris, E., Isaak, K. G., & Gao, Y. 2012, ApJ, 751, 10
Puech, M., Flores, H., Hammer, F., et al. 2008, A&A, 484, 173
Reis, R. C., Reynolds, M. T., Miller, J. M., & Walton, D. J. 2014, Nature, 507, 207
Riechers, D. A., Hodge, J., Walter, F., Carilli, C. L., & Bertoldi, F. 2011, ApJ, 739, L31
Riechers, D. A., Bradford, C. M., Clements, D. L., et al. 2013, Nature, 496, 329
Rieke, G. H., Young, E. T., Engelbracht, C. W., et al. 2004, ApJS, 154, 25
Robertson, B., Bullock, J. S., Cox, T. J., et al. 2006, ApJ, 645, 986
Sajina, A., Yan, L., Fadda, D., Dasyra, K., & Huynh, M. 2012, ApJ, 757, 13
Salpeter, E. E. 1955, ApJ, 121, 161
Sanders, D. B., & Mirabel, I. F. 1996, ARA&A, 34, 749
Skrutskie, M. F., Cutri, R. M., Stiening, R., et al. 2006, AJ, 131, 1163
Sluse, D., Surdej, J., Claeskens, J.-F., et al. 2003, A&A, 406, L43
Solomon, P. M., Downes, D., Radford, S. J. E., & Barrett, J. W. 1997, ApJ, 478, 144
Solomon, P. M., & Vanden Bout, P. A. 2005, ARA&A, 43, 677
Springel, V., & Hernquist, L. 2005, ApJ, 622, L9
Steinhardt, C. L., Schramm, M., Silverman, J. D., et al. 2012, ApJ, 759, 24
Stern, D., Eisenhardt, P., Gorjian, V., et al. 2005, ApJ, 631, 163
Swinbank, A. M., Smail, I., Bower, R. G., et al. 2005, MNRAS, 359, 401
Tacconi, L. J., Genzel, R., Smail, I., et al. 2008, ApJ, 680, 246
Tacconi, L. J., Genzel, R., Neri, R., et al. 2010, Nature, 463, 781
Ueda, J., Iono, D., Yun, M. S., et al. 2014, ApJS, 214, 1
Wilson, C. D., Petitpas, G. R., Iono, D., et al. 2008, ApJS, 178, 189
Wright, E. L., Eisenhardt, P. R. M., Mainzer, A. K., et al. 2010, AJ, 140, 1868
Yuan, T.-T., Kewley, L. J., & Sanders, D. B. 2010, ApJ, 709, 884